CrossMark

Statistical Properties of Ribbon Evolution and Reconnection Electric Fields in Eruptive and Confined Flares

J. Hinterreiter[1] (ID) · **A.M. Veronig[1,2]** · **J.K. Thalmann[1]** ·
J. Tschernitz[1] · **W. Pötzi[2]**

Abstract A statistical study of the chromospheric ribbon evolution in Hα two-ribbon flares was performed. The data set consists of 50 confined (62%) and eruptive (38%) flares that occurred from June 2000 to June 2015. The flares were selected homogeneously over the Hα and *Geostationary Operational Environmental Satellite* (GOES) classes, with an emphasis on including powerful confined flares and weak eruptive flares. Hα filtergrams from the Kanzelhöhe Observatory in combination with *Michelson Doppler Imager* (MDI) and *Helioseismic and Magnetic Imager* (HMI) magnetograms were used to derive the ribbon separation, the ribbon-separation velocity, the magnetic-field strength, and the reconnection electric field. We find that eruptive flares reveal statistically larger ribbon separation and higher ribbon-separation velocities than confined flares. In addition, the ribbon separation of eruptive flares correlates with the GOES SXR flux, whereas no clear dependence was found for confined flares. The maximum ribbon-separation velocity is not correlated with the GOES flux, but eruptive flares reveal on average a higher ribbon-separation velocity (by $\approx 10 \ \mathrm{km \, s^{-1}}$). The local reconnection electric field of confined ($cc = 0.50 \pm 0.02$) and eruptive ($cc = 0.77 \pm 0.03$) flares correlates with the GOES flux, indicating that more powerful

✉ J. Hinterreiter
juergen.hinterreiter@uni-graz.at

A.M. Veronig
astrid.veronig@uni-graz.at

J.K. Thalmann
julia.thalmann@uni-graz.at

J. Tschernitz
johannes.tschernitz@edu.uni-graz.at

W. Pötzi
werner.poetzi@uni-graz.at

[1] Institute of Physics, University of Graz, Universitätsplatz 5, 8010 Graz, Austria

[2] Kanzelhöhe Observatory for Solar and Environmental Research, University of Graz, Kanzelhöhe 19, 9521 Kanzelhöhe, Austria

flares involve stronger reconnection electric fields. In addition, eruptive flares with higher electric-field strengths tend to be accompanied by faster coronal mass ejections.

1. Introduction

Solar flares are powerful eruptions on the Sun and are characterized by rapid and intense variations of the Sun's irradiance over a wide range of the electromagnetic spectrum (*e.g.* review by Aschwanden, 2005; Fletcher *et al.*, 2011). They are powered by magnetic reconnection, during which the stored free magnetic energy in the corona is suddenly released. Solar flares present a large variety of morphological and evolutionary characteristics. They preferentially originate from complex magnetic-field configurations and may reveal complex flare-ribbon motion. In this article, we refer to flare events associated with an observed coronal mass ejection (CME) as *eruptive flares* and flares that are not associated with CMEs as *confined flares* (Švestka, 1986). The probability of flares being associated with CMEs increases steeply with the flare class. About 90% of X-class flares are eruptive (Yashiro *et al.*, 2006; Wang and Zhang, 2007), and all flares ≥ X5 tend to have an associated CME.

The most widely accepted reconnection model for eruptive flares is the so-called CSHKP model (Carmichael, 1964; Sturrock, 1966; Hirayama, 1974; Kopp and Pneuman, 1976). It is intrinsically a 2.5D approach that assumes translation symmetry and successfully explains characteristic features of eruptive flares, such as quasi-parallel ribbons and their increasing separation in the course of a flare. Recently, 3D numerical simulations have further increased our understanding of the physical processes involved (*e.g.* Aulanier, Janvier, and Schmieder, 2012; Janvier *et al.*, 2014). Within the CSHKP framework, a magnetic-flux system may become unstable and slowly rise to higher coronal altitudes. Below it, a current sheet develops, toward which the ambient magnetic field is drawn and forced to reconnect (Vršnak, 1990). The energy released heats the local coronal plasma and accelerates particles to nonthermal energies. A significant fraction of the energy is transported toward the low solar atmosphere along newly reconnected flare loops by nonthermal electrons. They produce enhanced emission at hard X-rays (HXR) by thick-target bremsstrahlung in the low atmosphere (see Emslie, 2003 and Fletcher *et al.*, 2011, respectively). While the HXR emission is most often observed in the form of localized kernels ("HXR footpoints"), the EUV, UV, and Hα emission often appears in the form of elongated ribbons. They can be formed by the fast electron beams as well as by thermal conduction from the hot flaring corona. Importantly, flare kernels and ribbons may thus be regarded as tracers of the low-atmosphere footpoints of newly reconnected coronal magnetic fields. As the reconnection region moves upward, field lines anchored at successively larger distances from the polarity inversion line (PIL) are swept into the current sheet and reconnect. Thus, the ribbons appear farther away from the PIL as the flare-loop system grows, leading to an apparent expansion motion of the Hα flare ribbons (Fletcher *et al.*, 2011). In contrast to eruptive flares, confined flares show only a short range of separation motion of the two flare ribbons (Kurokawa, 1989), indicating that the reconnection region is not moving upward.

The generation of a reconnecting current sheet is essential for the energy release in a solar flare, because the free magnetic energy stored in the corona can be dissipated and lead to

particle acceleration and plasma heating (Martens and Young, 1990; Litvinenko and Somov, 1995). A general measure of the rate of magnetic reconnection is the electric voltage drop [$\dot{\varphi}_c$] along the reconnecting current sheet, which is related to the net change in magnetic flux. Forbes and Lin (2000) showed that the global reconnection rate can be obtained from observations as follows:

$$\dot{\varphi}_c = \frac{d\varphi_c}{dt} = \int E_c \, dl = \frac{\partial}{\partial t} \int B_n \, da, \tag{1}$$

where E_c is the local electric field in the coronal reconnection region, dl is the length along the current sheet, aligned in the direction of the ribbon, B_n is the component of the magnetic field normal to the photosphere, and da is the newly brightened area swept by the flare ribbons. Assuming that neither the magnetic field nor the length of the ribbons changes significantly during a flare, one can rewrite Equation 1 as follows (see Forbes and Lin, 2000 and references therein):

$$\dot{\varphi}_c = \int v_r B_n \, dl, \tag{2}$$

where v_r is the ribbon-separation velocity. Qiu *et al.* (2002) pointed out that for a two-ribbon flare with a 2D configuration (*i.e.* translation symmetry along the ribbon) and the line-tying nature of the photospheric magnetic field, Equations 1 and 2 reduce to (see also Forbes and Priest, 1984; Forbes and Lin, 2000)

$$E_c = v_r B_n, \tag{3}$$

where E_c can be interpreted as a local reconnection rate.

When applying Equation 3, the outer front of the flare ribbons should be considered, because this part is related to the newly reconnected field lines along which the accelerated particles travel downward to the solar surface. Since the flare ribbons are tracked using chromospheric images, the chromospheric magnetic field should also be used to determine the reconnection electric field using Equation 3. In practice, however, the chromospheric magnetic field is difficult to measure, so that, generally, photospheric magnetic-field maps are used to retrieve the reconnection rates.

Equation 3 was applied in various case studies of solar flares (Poletto and Kopp, 1986; Qiu *et al.*, 2002; Asai *et al.*, 2004; Temmer *et al.*, 2007; Miklenic *et al.*, 2007). Liu and Wang (2009) and Jing *et al.* (2005) each performed statistical studies of powerful and mainly eruptive flares. In both studies, the authors found a clear dependence of the local coronal electric field on the strength of the flare as indicated by the soft X-ray (SXR) peak flux measured by the *Geostationary Operational Environmental Satellite* (GOES).

In this article we present the first systematic statistical study comparing the electric field in the reconnecting current sheet in eruptive and confined flares using a homogeneous data set that spans more than one solar cycle. The set covers 50 events in total, ranging from GOES classes B to > X10, including 19 eruptive and 31 confined flares.

2. Data and Data Reduction

The data set consists of 50 Hα flares, selected to contain all powerful flares and an appropriate number of weaker flares (eruptive and confined) that originated from close to the central meridian and were observed in full-disk Hα filtergrams at the Kanzelhöhe Observatory for Solar and Environmental Research (KSO; kso.ac.at) between June 2000 and June 2015.

Figure 1 Distribution of the selected flares (50 in total: 19 eruptive, and 31 confined). *Blue* (*backward diagonal hatching*) and *red* (*forward diagonal hatching*) bars correspond to eruptive and confined flares, respectively.
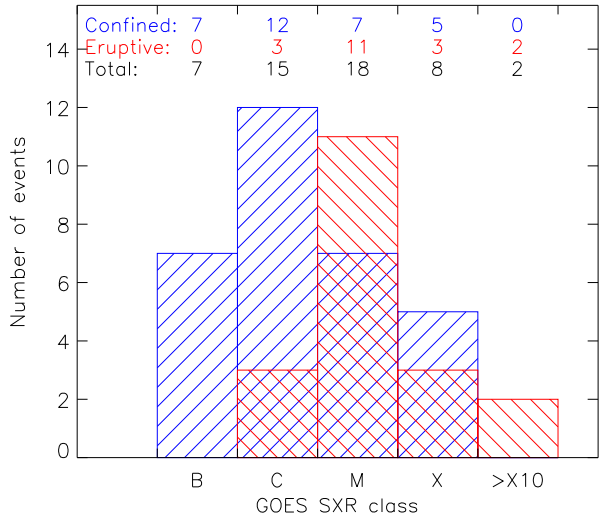
We aimed at having good coverage over Hα and GOES classes with a balance between confined and eruptive flares. Figure 1 shows the distribution of the selected flares over the GOES class. First we searched for all flares of Hα classification (sidc.be/educational/classification.php#OClass) 4 and 3. Then an appropriate number of importance class 2 flares were selected. For the importance class 1 and S flares, we searched for suitable flares beginning from 2015 and going backward in time. In addition, we placed an emphasis on including powerful confined as well as weak eruptive flares. The flares were selected to be close to the center of the solar disk (CMD $< 45°$), in order to minimize projection effects. The central meridian distance (CMD) is the angular distance in solar longitude measured from the central meridian.

The *Solar and Heliospheric Observatory/Large Angle and Spectrometric Coronagraph* (SOHO/LASCO) CME catalog (cdaw.gsfc.nasa.gov/CME_list) was checked to determine the flare–CME association. The flare position had to be consistent with the position angle given in the CME catalog and the flare had to occur within 60 minutes of the linearly extrapolated starting time of the CME. For the M1.2/1N flare on 1 October 2011, an eruption in the original LASCO movie can be seen, but no entry in the SOHO/LASCO CME catalog exists. We therefore refer to Temmer *et al.* (2017), who reported a CME speed of 450 km s^{-1}.

To track the flare-ribbon-separation motion, we used Hα full-disk data obtained at the KSO. The KSO Hα telescope is a refractor with an aperture ratio of d/f = 100/2000 equipped with a Lyot filter centered at 6563 Å and a FWHM of 0.7 Å. For the time range June 2000 to April 2008, the resolution of the images was about 2.2″ (8-bit CCD until mid-2005 and 10-bit CCD after) with a temporal cadence of roughly one minute. Since April 2008, KSO has obtained high-resolution (approximately 1″, 12-bit CCD) and high-cadence (roughly six seconds) filtergrams. In addition, all images have to pass a primary quality check (Pötzi *et al.*, 2015). In order to also include the most powerful flares during this time range, we used Hα data from other observatories as well. To analyze the X17.2/4B flare on 28 October 2003, we used high-resolution Hα filtergrams obtained by the Udaipur Solar Observatory (USO) with a 15 cm aperture f/15 telescope and a 12-bit CCD. The temporal cadence of the images is approximately 30 seconds and the pixel scale was derived by coalignment with KSO data, which partially covered the event, resulting in 0.6 arcsec. The

images for the X10.0/2B flare on 29 October 2003 are provided by the National Solar Observatory at Sacramento Peak. They were obtained by a 12-bit CCD camera with a pixel size of about one arcsec and a temporal cadence of about one minute (Neidig *et al.*, 1998).

To calculate the coronal electric field, measurements of the photospheric magnetic field are required. Therefore, we used 96-minute cadence full-disk magnetograms from the *Michelson Doppler Imager* (MDI: Scherrer *et al.*, 1995) onboard SOHO for flares before 2011 and low-noise 720-second cadence magnetograms from the *Helioseismic and Magnetic Imager* onboard the *Solar Dynamics Observatory* (SDO/HMI: Schou *et al.*, 2012) for flares since 2011. For each event we selected the latest available magnetogram before the flare start.

Furthermore, the GOES SXR light curves in the $1-8$ Å band were used to quantify the flare energy release. In order to determine the timing of the strongest energy deposition, we used the derivative of the GOES SXR flux according to the so-called Neupert effect (Neupert, 1968; Veronig *et al.*, 2005). Table 1 lists the selected flares, together with additional information (times, position, class of the flares, and associated CMEs).

All of the images were rotated to Solar North and were corrected for solar differential rotation. A subregion around the flare area was selected, and all of the Hα filtergrams were coaligned with the first image of the time series using cross-correlation techniques. The MDI and HMI magnetograms were rebinned to the pixel scale of the Hα images and were coaligned with the first Hα filtergram of the sequence, using the corresponding MDI or HMI continuum images. In addition, the Hα images were normalized and filtered in order to handle large-scale intensity differences, *i.e.* darkening due to clouds (for a detailed description see Pötzi *et al.*, 2015 and Tschernitz *et al.*, 2017). All data were prepared and reduced using the instrument data reduction routines in the SolarSoft distribution.

3. Analysis

In the following, the method that we used to track the flare ribbons is shown using two example flares. The first example flare is the M1.1/2N eruptive flare on 9 November 2011 (see Figure 2). From the pre-flare HMI line-of-sight (LOS) magnetic field we retrieved the flare-relevant polarity inversion line (PIL) using the IDL contour procedure. We then manually selected a position along the PIL from which we tracked the ribbon motion. When possible, the slit locations were selected in such a way that both flare ribbons were well pronounced and could be tracked simultaneously in a direction perpendicular to the PIL. The white line in Figure 2 represents the PIL, and the red line is a linear fit to the PIL, locally around the chosen position. The yellow rectangle indicates the subregion (length of $200''$ and width of $6''$) used to track the ribbons, perpendicular to the local PIL. The top panels in Figure 3 show the extracted subregions within the Hα maps for six time steps, and the bottom panels show the mean-intensity profiles derived along the extracted subregions. For this purpose, the mean value of each pixel column was calculated and fitted by a Gaussian (red curve). We derived the position of the leading front (vertical green line) of the ribbon by taking the peak of the Gaussian fit (vertical dashed-blue line) plus 2σ. For a detailed description of the Gaussian fit function and the uncertainties see Appendix A.

Figure 4 shows the summary plot of the flare-ribbon detection and analysis for the northern ribbon alone (*cf.* Figure 2), *i.e.* for the intensity profiles shown on the right side of the PIL in Figure 3. In Figure 4a we plot the GOES $1-8$ Å SXR flux (black) and its temporal derivative (thick red). Figure 4b shows the distance of the flare-ribbon leading front with respect to the PIL. Since we are interested in the overall ribbon motion and to improve the

Table 1 Results of ribbon tracking for all flares under study. We list the date, KSO flare times, flare classification (Hα and GOES), heliographic position (u is the angular distance to the solar disk center), and CME properties. The CME speed is the linear speed from the LASCO catalog. The ribbon distance is the minimum and maximum distance of the flare ribbons. Ribbon-separation velocity gives the maximum speed of the faster ribbon. B_E is the magnetic field at the leading front of the flare ribbon at the time of the maximum electric field. E_c is the maximum electric field.

| Date | KSO times | | | Class | | Position | u | CME | Ribbon distance | | Velocity | B_E | E_c |
	Start [UT]	Max [UT]	End [UT]	Hα	GOES	Lat. Lon	[°]	Speed [km s⁻¹]	Min [Mm]	Max [Mm]	Max [km s⁻¹]	[G]	Max [V cm⁻¹]
01 Jun. 2000	07:30	07:32	08:18	2N	C8.2	S13E24	27.4	–	11.8 ± 4.0	38.4 ± 4.3	23.9 ± 10.6	623	10.6 ± 3.1
19 Jul. 2000*	06:37	07:23	09:01	3N	M6.4	S15E07	12.3	–	15.3 ± 7.0	42.4 ± 4.6	13.0 ± 8.4	1618	15.6 ± 13.9
12 Sep. 2000	11:22	12:00	14:58	2F	M1.0	S19W08	14.1	1550	51.5 ± 5.6	73.7 ± 4.6	10.4 ± 6.9	231	2.3 ± 1.1
25 Aug. 2001	16:23	16:32	17:25	3N	X5.3	S21E38	39.3	1433	48.3 ± 6.6	83.9 ± 5.6	23.7 ± 12.1	1318	28.4 ± 6.9
26 Oct. 2003*	06:46	06:46	09:17	3B	X1.2	S14E41	41.4	1371	35.0 ± 3.9	46.2 ± 4.0	7.3 ± 8.8	1497	6.0 ± 8.1
28 Oct. 2003	10:32	11:23	14:20	4B	X17.2	S16E07	13.2	2459	14.7 ± 0.9	65.4 ± 1.0	56.5 ± 4.2	1693	68.1 ± 3.4
29 Oct. 2003	20:37	20:42	22:53	2B	X10.0	S15W02	10.6	2029	21.5 ± 2.4	54.8 ± 3.9	25.2 ± 5.8	2389	60.3 ± 7.2
18 Nov. 2003	07:30	07:50	11:04	3N	M3.2	S02E37	37.0	1660	42.7 ± 4.9	63.6 ± 4.8	45.8 ± 9.1	683	21.9 ± 2.8
20 Nov. 2003	07:35	07:42	08:43	3B	M9.6	N01W08	8.6	669	18.8 ± 5.8	73.3 ± 6.4	38.0 ± 14.6	412	13.3 ± 3.1
16 Jul. 2004	13:50	13:57	14:31	4B	X3.6	S09E29	29.1	–	58.7 ± 3.3	78.3 ± 3.3	29.4 ± 11.5	565	10.5 ± 5.7
17 Jul. 2004	07:54	08:05	08:53	2F	X1.0	S11E22	22.7	–	50.8 ± 3.3	56.3 ± 3.3	12.1 ± 14.1	585	6.8 ± 4.1
20 Jul. 2004	12:26	12:31	13:30	3B	M8.6	N10E32	35.2	710	22.7 ± 3.3	53.5 ± 3.3	37.6 ± 15.1	632	19.4 ± 4.7
15 Jan. 2005	11:46	11:51	12:00	2F	M1.2	N13E01	8.4	–	34.4 ± 5.8	46.0 ± 5.2	20.4 ± 13.7	2418	19.0 ± 15.8
17 Jan. 2005	07:16	09:51	11:57	3B	X3.8	N14W24	25.4	2547	17.5 ± 8.5	70.1 ± 5.8	46.4 ± 9.1	1360	42.7 ± 11.3
12 May 2005	07:28	07:34	08:57	2B	M1.6	N12E28	29.2	–	53.7 ± 4.5	68.4 ± 4.4	39.0 ± 14.8	207	3.0 ± 1.6
12 Sep. 2005	08:42	08:49	11:05	3N	M6.1	S13E25	25.3	–	14.0 ± 3.9	42.7 ± 6.2	39.5 ± 12.1	204	8.0 ± 2.5
15 Sep. 2005*	08:34	08:40	10:10	2N	X1.1	S11W15	15.3	–	38.7 ± 5.2	42.7 ± 4.0	4.2 ± 12.4	805	3.1 ± 4.6
06 Jul. 2006	08:16	08:42	10:24	3N	M2.5	S10W30	30.5	911	40.0 ± 4.9	71.8 ± 5.2	62.9 ± 22.5	683	42.9 ± 8.3
07 Mar. 2011	13:48	14:31	14:50	2F	M1.9	N10E18	18.0	698	30.9 ± 1.6	50.7 ± 2.1	14.5 ± 7.1	160	2.0 ± 0.6
22 Apr. 2011*	11:09	11:33	12:02	2N	C7.7	S16E34	39.7	–	25.1 ± 2.1	31.6 ± 1.5	7.5 ± 7.5	761	5.7 ± 2.9
02 Jun. 2011	07:25	07:47	08:11	2N	C3.7	S19E20	27.7	976	23.9 ± 1.9	37.3 ± 2.7	9.1 ± 8.8	403	2.1 ± 1.1
28 Sep. 2011	12:29	12:34	12:55	1N	C9.3	N15W01	21.9	–	38.0 ± 1.5	46.6 ± 1.5	26.1 ± 6.3	92	2.0 ± 3.6
01 Oct. 2011	09:23	10:00	10:38	1N	M1.2	N08W03	15.0	450	16.6 ± 2.9	39.0 ± 1.5	29.2 ± 6.7	1322	22.9 ± 3.8
09 Nov. 2011	13:06	13:27	14:15	2N	M1.1	N22E36	43.5	907	27.9 ± 1.5	68.1 ± 1.5	59.2 ± 6.1	134	5.9 ± 1.6

Table 1 ((*Continued.*))

Date	KSO times Start [UT]	Max [UT]	End [UT]	Class Hα	GOES	Position Lat. Lon	u [°]	CME Speed [km s⁻¹]	Ribbon distance Min [Mm]	Max [Mm]	Velocity Max [km s⁻¹]	B_E [G]	E_c Max [V cm⁻¹]
06 Mar. 2012	12:23	12:40	13:26	2N	M2.1	N17E35	35.5	–	11.2 ± 2.3	17.2 ± 2.2	17.1 ± 5.9	822	12.0 ± 2.8
15 Mar. 2012	07:25	07:45	08:45	2F	M1.8	N14E00	6.8	485	28.2 ± 2.1	47.5 ± 2.7	22.7 ± 8.3	589	11.3 ± 1.8
27 Apr. 2012	08:11	08:21	08:42	1N	M1.0	N12W30	30.6	–	19.6 ± 1.5	28.2 ± 2.4	17.6 ± 6.4	572	1.3 ± 1.4
10 Jul. 2012	06:10	06:23	07:34	1F	M2.1	S16E30	31.9	–	8.6 ± 5.2	12.7 ± 1.5	3.1 ± 7.0	873	2.7 ± 3.1
11 Apr. 2013	06:56	07:08	09:15	3B	M6.5	N08E14	14.1	861	18.0 ± 2.1	47.0 ± 1.9	39.1 ± 5.2	354	10.4 ± 1.7
09 Jul. 2013	13:27	13:32	13:48	SN	C2.3	S10W21	21.7	–	35.0 ± 1.5	42.2 ± 1.5	4.4 ± 5.6	613	1.7 ± 2.1
02 Aug. 2013	11:10	11:11	11:24	SF	B9.7	S15W10	13.4	–	13.0 ± 2.3	16.5 ± 2.5	5.0 ± 7.2	125	0.5 ± 0.4
11 Aug. 2013*	12:29	12:31	12:42	SF	B7.1	S21E31	33.3	–	24.9 ± 2.0	28.9 ± 8.2	8.0 ± 11.7	418	3.3 ± 2.5
23 Sep. 2013*	07:10	07:11	07:24	SF	B6.0	N10E35	38.8	–	27.9 ± 1.5	31.5 ± 7.8	17.6 ± 9.1	104	1.8 ± 0.7
16 Oct. 2013	09:12	09:20	09:44	SF	C1.9	S09W42	41.8	–	14.3 ± 2.1	18.2 ± 2.1	2.1 ± 4.4	305	0.6 ± 0.7
20 Oct. 2013	08:36	08:41	09:08	1N	C2.9	N22W32	41.7	398	17.0 ± 1.6	31.9 ± 1.6	35.8 ± 10.2	226	5.1 ± 1.3
29 Nov. 2013	09:55	10:10	10:14	1F	C1.5	S06W23	23.5	–	12.4 ± 6.8	18.1 ± 2.8	7.6 ± 8.3	35	0.1 ± 0.1
14 Dec. 2013	11:06	11:19	11:58	1F	C2.3	S14W14	20.3	–	37.9 ± 1.5	44.6 ± 1.5	4.7 ± 7.1	332	1.4 ± 1.1
28 Dec. 2013	12:42	12:44	13:05	1F	C3.0	S17E10	21.9	–	16.7 ± 1.9	23.5 ± 3.1	12.2 ± 6.7	316	3.6 ± 1.5
14 Feb. 2014	10:38	10:40	11:04	1N	C7.2	S11W29	33.9	–	28.2 ± 1.5	37.1 ± 6.2	11.6 ± 5.7	1295	13.6 ± 3.7
21 Mar. 2014	10:18	10:35	11:01	1F	C2.7	N17E39	39.3	423	28.6 ± 5.3	42.4 ± 2.8	5.7 ± 4.7	436	1.8 ± 1.2
02 May 2014	09:17	09:23	10:19	1N	C4.4	S19W16	27.9	–	20.6 ± 1.5	34.4 ± 1.6	14.7 ± 7.5	1282	8.4 ± 4.8
10 May 2014	06:51	07:01	08:02	2N	C8.7	N03E27	27.0	–	13.9 ± 3.0	39.8 ± 2.8	32.5 ± 5.2	836	22.5 ± 2.4
12 May 2014	06:25	06:38	07:07	1F	C2.3	N04W02	2.2	–	15.5 ± 4.0	31.2 ± 1.5	26.7 ± 6.5	118	2.1 ± 0.5
21 Jun. 2014	13:36	13:54	14:03	SF	B4.7	S11E04	10.1	–	32.8 ± 1.6	40.7 ± 2.8	8.4 ± 3.8	675	5.5 ± 1.9
26 Jun. 2014	07:12	07:31	07:46	SN	B3.1	N10E30	32.3	–	25.0 ± 1.9	32.1 ± 1.5	7.6 ± 9.7	66	0.4 ± 0.3
10 Aug. 2014	10:05	10:07	10:14	SF	B8.9	S21W12	18.7	–	23.8 ± 4.6	34.5 ± 2.5	26.9 ± 19.2	545	7.9 ± 2.6
22 Oct. 2014*	14:02	14:06	14:55	3B	X1.6	S14E15	17.2	–	47.0 ± 2.6	52.6 ± 2.0	6.1 ± 7.6	991	6.0 ± 3.8
26 Oct. 2014*	10:03	10:51	10:51	2N	X2.0	S14W34	34.7	–	27.8 ± 1.5	29.2 ± 1.7	3.1 ± 6.7	1750	5.5 ± 5.9
02 Nov. 2014	13:07	13:11	13:19	SF	B7.6	S04E29	28.9	–	16.0 ± 8.2	22.5 ± 4.6	6.6 ± 4.4	393	1.5 ± 2.2
25 Jun. 2015*	08:02	08:14	12:00	3B	M7.9	N11W41	42.9	1627	21.9 ± 1.9	40.1 ± 2.6	10.3 ± 10.0	1424	10.7 ± 0.9

*Tracking of the two flare ribbons is done separately because the ribbons do not lie *vis-à-vis* each other (see Figure 6 for an example).
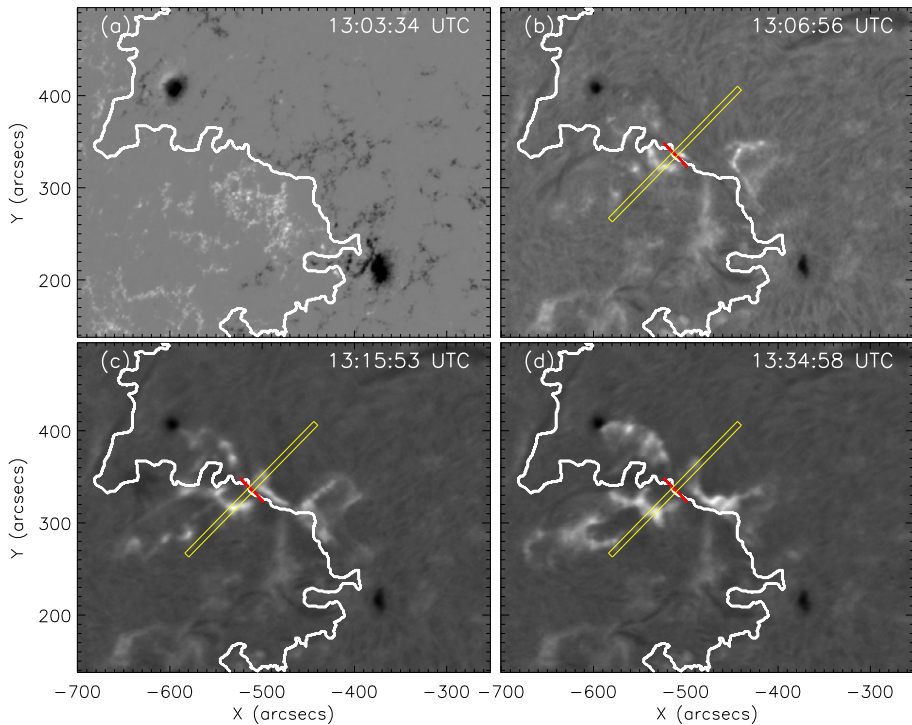
Figure 2 M1.1/2N eruptive flare on 9 November 2011. (**a**) LOS magnetic field scaled to ±1000 G with the PIL indicated by the *white line*. (**b**)–(**d**) Three Hα images at different times. The *white line* is the PIL, and the *red line* is a linear fit of the local PIL. The *yellow rectangle* is perpendicular to the locally fitted PIL, indicating the direction in which the ribbons are tracked. See Movie1.mp4 in the Electronic Supplementary Material.

statistics, we binned the distance values over intervals covering 30 seconds and performed a polynomial fitting to the distance–time curve. For this particular flare, a polynomial fit of tenth order was used. The velocities of the flare-ribbon separation for the leading front was obtained by the time derivative of the polynomial fit to the distance–time data (*cf.* Figure 4c). Figure 4d shows the underlying mean magnetic field at the position of the leading front of the flare ribbon, assuming an uncertainty of 20 G. In order to account for projection effects, we applied a correction of $B_n = B_{LOS}/\cos(u)$, where u is the angular distance to the solar disk center, and B_{LOS} is the LOS magnetic-field strength. u is calculated using the heliographic latitude and heliographic longitude listed in the KSO flare reports. Figure 4e shows the reconnection electric field, which is derived using Equation 3.

This flare shows a correlation of the ribbon-separation velocity and the derivative of the GOES flux. At the time when the derivative of the GOES flux has its maximum, the ribbons are moving faster away from the PIL, reaching speeds of up to 60 km s^{-1}. With a relatively weak underlying photospheric magnetic field, which has a maximum of about 150 G, we obtain a maximum electric field of roughly 6 V cm^{-1}. The evolution of the electric field seems to be more affected by the magnetic field swept by the flare ribbons than by the ribbon-separation velocity (*cf.* Figure 4c – e).

The particular choice of the direction used to follow the flare ribbons on either side of the PIL may influence our results, including the minimum/maximum separation, the separation
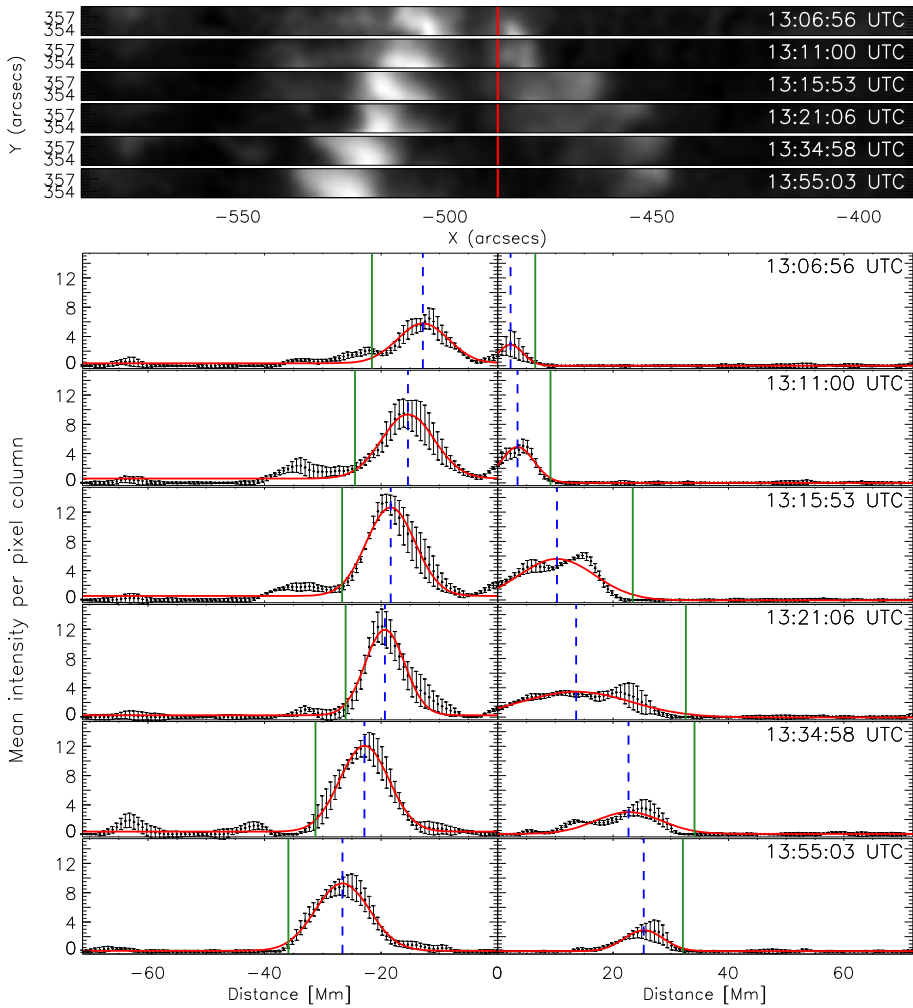
Figure 3 *Top panels*: Selected subregion (*cf. yellow rectangle* in Figure 2) that was used to track the flare ribbons of the M1.1/2N eruptive flare on 9 November 2011, shown for six time steps. The *vertical red line* indicates the PIL. *Bottom panels*: Intensity profiles for the local flare ribbon on both sides of the PIL, derived from the subregion plotted at the top. Zero-value indicates the position of the PIL. The *black points* with the *error bars* represent the mean-intensity values, and the errors are the standard deviation of the pixel intensities in one column. *Red curve*: Gaussian fit. *Vertical dashed-blue line*: Peak of the Gaussian fit. *Vertical green line*: Front of the Gaussian fit (defined as peak plus 2σ). See Movie2.mp4 and Movie3.mp4 in the Electronic Supplementary Material.

speed, and most importantly, the maximum electric field. In order to assess the effect of the particular choice, we applied four different ribbon-tracking directions for the M1.1/2N eruptive flare on 9 November 2011 (see Figure 5a). In Figure 5b the maximum electric field deduced for the individual tracking directions is shown, ranging between $4\,\mathrm{V\,cm^{-1}}$ and $6\,\mathrm{V\,cm^{-1}}$ and appearing to be quite a robust measure.

There are events in our sample, however, for which we cannot use a single slit to follow the flare ribbons simultaneously on either side of the PIL. As an example of such a case,
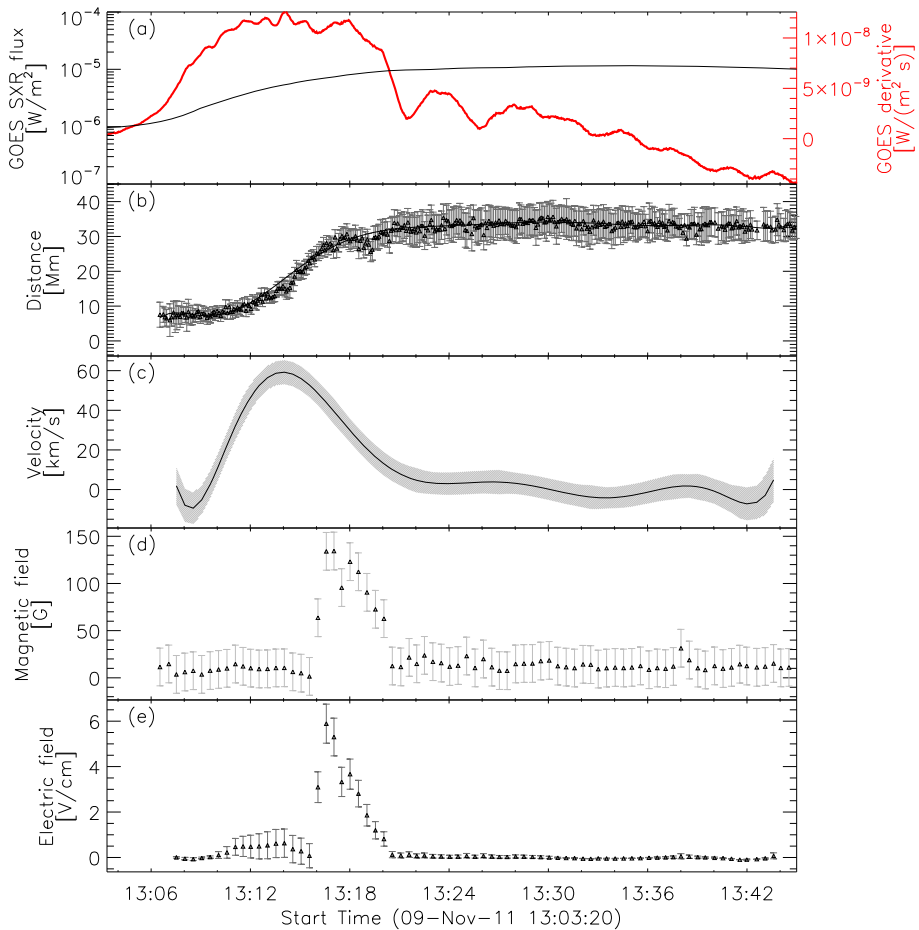
Figure 4 Flare parameters determined for the northern (right) ribbon of the M1.1/2N eruptive flare on 9 November 2011. From top to bottom: (**a**) GOES $1–8$ Å SXR flux (*black curve*) and its derivative (*thick red curve*). (**b**) Distance of the ribbon for each time step with uncertainties and the corresponding polynomial fit. (**c**) Separation velocity of the ribbon with uncertainties. (**d**) Binned LOS magnetic-field values at the positions of the leading front with uncertainties. (**e**) Calculated flare electric field for the leading front with uncertainties.

we show snapshots of the X1.6/3B flare on 22 October 2014 (for details see Table 1) in Figure 6. The ribbons do not appear *vis-à-vis* each other, considering any direction perpendicular to the PIL, but they are strongly sheared. In such cases, we used different tracking directions for the two ribbons (see Figure 6d). While the negative-polarity (eastern) ribbon was tracked within the subregion outlined by the yellow rectangle (see also Figure 7), we used the subregion outlined in blue for the analysis of the positive-polarity (western) ribbon. Figure 8 shows the summary plot for the eastern ribbon of the X1.6/3B confined flare on 22 October 2014. It shows that the ribbon only marginally separates from the PIL and the peak of the separation velocity is ≈ 6 km s^{-1}. However, the ribbons cover a region with a strong underlying magnetic field (up to 1600 G; see also Veronig and Polanec, 2015) and therefore, in this event the maximum electric field also reaches 6 V cm^{-1}.
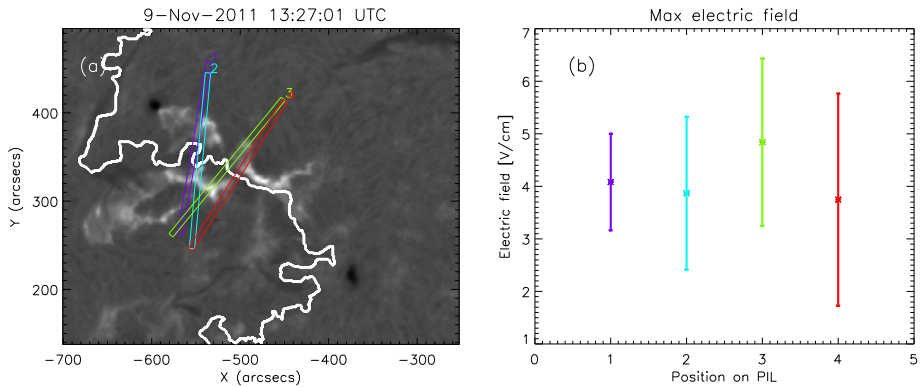
Figure 5 (**a**) Hα snapshot of the M1.1/2N eruptive flare on 9 November 2011 at the peak time. The *rectangles in different colors* represent the different directions perpendicular to the PIL (in *white*) that were used to track the flare ribbons. (**b**) Maximum electric-field strength along different positions perpendicular to the PIL.

4. Results

The analysis described in Section 3 has been performed for all flares of our event sample. For the statistical analysis we derived the minimum ribbon distance, the maximum ribbon distance, the maximum ribbon-separation velocity, the peak photospheric magnetic-field strength swept by the flare ribbons, and the maximum coronal electric field. We obtained the minimum ribbon distance by summing the minimum distance derived from the polynomial fits to the time–distance curves (*cf.* Figure 4b) for both flare ribbons. Hence, this gives an estimate of the ribbon distance at the start of the flare. The same procedure was applied for the maximum ribbon distance, but this time the maximum distance derived from the polynomial fits was summed. The ribbon separation indicates how far the ribbons move apart from each other and was calculated by subtracting the minimum ribbon distance from the maximum ribbon distance. To calculate the maximum ribbon-separation speed, we compared the maximum separation velocities of both ribbons and considered only the faster ribbon (*cf.* Figure 4c). To represent a characteristic value for the underlying photospheric magnetic field, we took the magnetic-field strength at the front of the flare ribbon at the time when the coronal electric field (calculated using Equation 3) had its maximum, *i.e.* at the time of the peak in Figure 4e. Therefore, it is termed B_{E} in the following. We note that the product of the maximum ribbon-separation speed and the magnetic field does not necessarily result in the maximum electric field. This is because the highest ribbon-separation speeds may not necessarily occur at the same time as when the ribbons are anchored in the strongest magnetic fields. The results for all the flares under study are summarized in Table 1.

   As explained above, there are events whose flare ribbons do not appear *vis-à-vis* the PIL, but are strongly sheared (see Figure 6 for an example). In such cases (indicated by an asterisk in Table 1), we performed the ribbon analysis separately along two different paths (one for each polarity region). In these cases the values for minimum and maximum ribbon distance do not give the actual distance of the ribbons, but represent the sum of the individually tracked ribbons, with respect to the PIL.
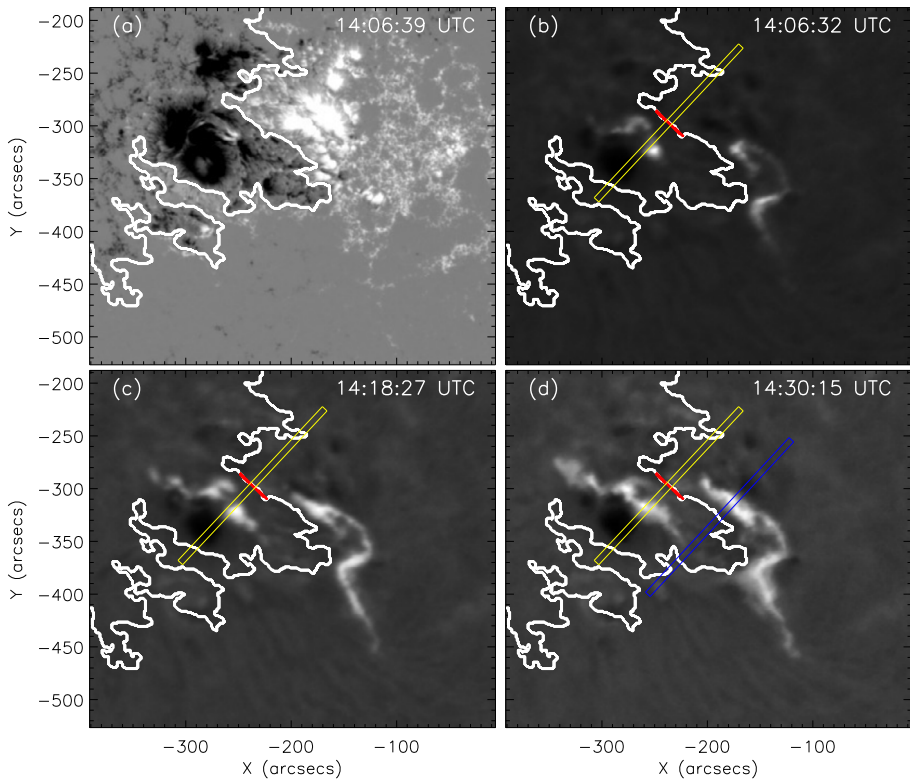
Figure 6 X1.6/3B confined flare on 22 October 2014. (**a**) LOS magnetic field scaled to ±1000 G with the PIL indicated by the *white line*. (**b**) – (**d**) Three Hα images of different times. The *white line* shows the PIL, the *red line* represents a linear fit of the local PIL, and the *yellow rectangle* is perpendicular to the locally fitted PIL, indicating the direction in which the ribbons are tracked. In panel **d** the tracking direction of the western ribbon is indicated by the *blue rectangle*.

4.1. Distributions of the Flare-Ribbon Parameters

Figure 9a shows the distribution of the ribbon separation, indicating how far the ribbons move apart from each other during the flare. All of the eruptive flares reveal ribbon separations > 10 Mm. Approximately 40% of eruptive flares even show a ribbon separation > 30 Mm. In contrast to eruptive flares, about 70% of the confined flares reveal a ribbon separation < 10 Mm; no confined flare shows a ribbon separation > 30 Mm.

Figure 9b presents the distribution of the maximum ribbon-separation speeds. Eruptive flares show a broad range, from 3 km s^{-1} up to 63 km s^{-1}. Twenty percent of the eruptive flares have maximum ribbon-separation velocities > 40 km s^{-1}, while the separation speeds of the flare ribbons in confined events never seem to exceed ≈ 40 km s^{-1}.

For 38 out of 50 flares, the strength of the photospheric magnetic field swept by the flare ribbons is < 1000 G (Figure 9c). The distribution for confined and eruptive flares is similar, indicating that both can appear in either weak or strong magnetic fields. B_{E} can reach values of up to almost 2500 G (M1.2/2F confined flare on 15 January 2005).
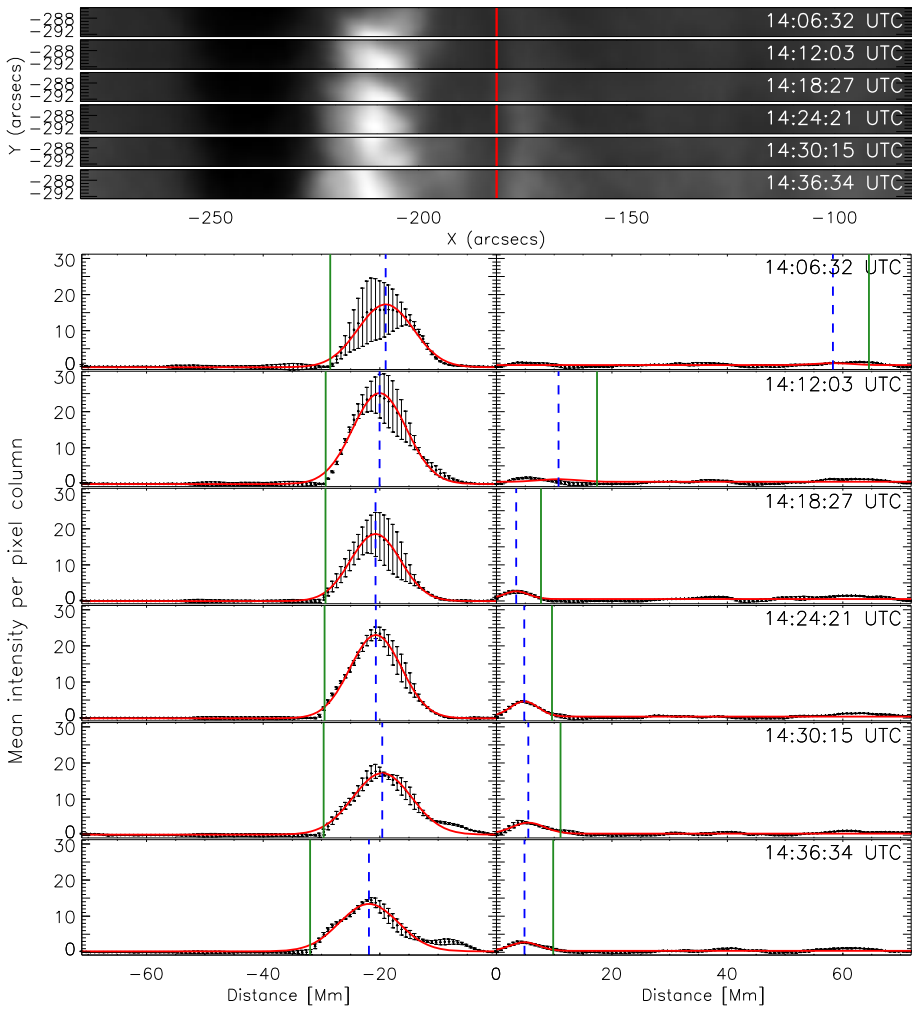
Figure 7 *Top panels*: Selected subregion (*cf. yellow rectangle* in Figure 6) that we used to track the flare ribbons of the X1.6/3B confined flare on 22 October 2014, shown for six time steps. The *vertical red line* indicates the PIL. *Bottom panels*: intensity profiles for the local flare ribbon on both sides of the PIL, derived from the subregion plotted at the *top*. Zero-value indicates the position of the PIL. The *black points* with the *error bars* represent the mean-intensity values, and the errors are the standard deviation of the pixel intensities in one column. *Red curve*: Gaussian fit. *Vertical dashed-blue line*: peak of the Gaussian fit. *Vertical green line*: front of the Gaussian fit (defined as peak plus 2σ). Note that in this case of very sheared flare ribbons, only the left side of the PIL was evaluated.

Figure 9d shows that roughly 50% of the confined flares have an electric-field strength < 5 V cm^{-1}, and E_c of only one confined flare exceeds 20 V cm^{-1}. Except for four eruptive flares, E_c is only found in the range of values lower than 30 V cm^{-1}. We find a mean electric-field strength of 6.0 ± 5.7 V cm^{-1} for confined flares and 19.9 ± 20.1 V cm^{-1} for eruptive flares. The electric-field strengths obtained in this study range from ≈ 0.1 V cm^{-1} (C1.5/SF confined flare on 29 November 2013) up to ≈ 70 V cm^{-1} for the most powerful flare under study (X17.2/4B flare on 28 October 2003), covering almost two orders of magnitude.
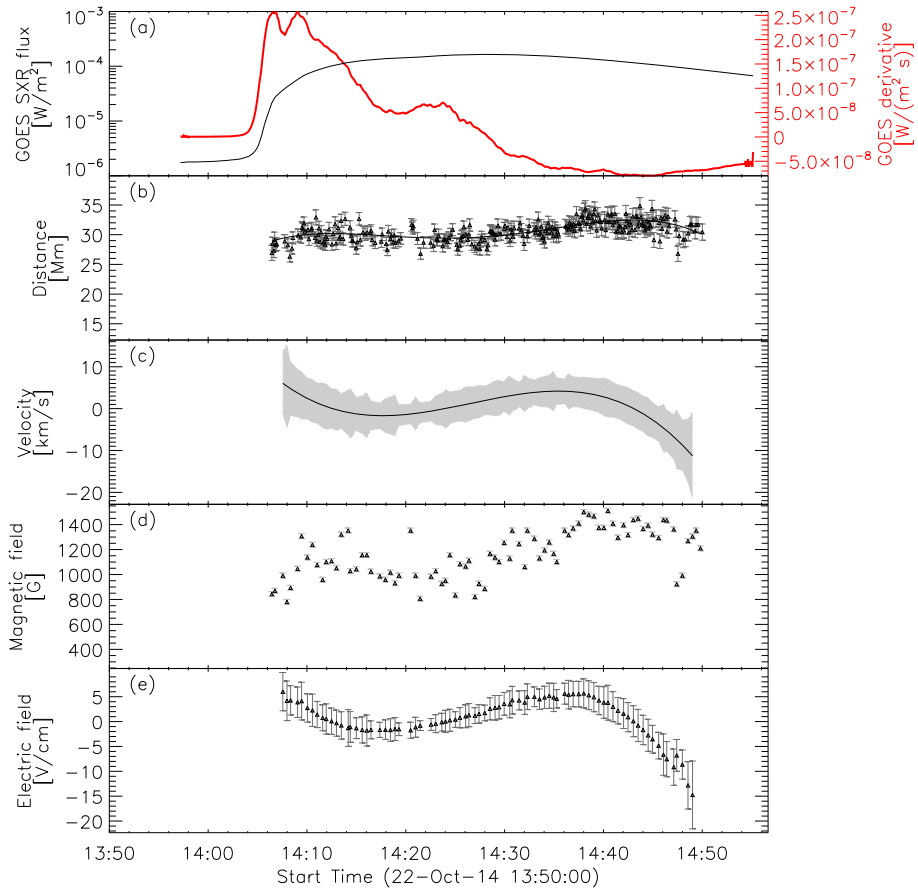
Figure 8 Flare parameters determined for the eastern (*left*) ribbon of the X1.6/3B confined flare on 22 October 2014. From top to bottom: (**a**) GOES 1 – 8 Å SXR flux (*black curve*) and its derivative (*thick red curve*). (**b**) Distance of the ribbon for each time step with uncertainties and the corresponding polynomial fit. (**c**) Separation velocity of the ribbon with uncertainties. (**d**) Binned LOS magnetic-field values at the positions of the leading front with uncertainties. (**e**) Calculated flare electric field for the leading front with uncertainties. The ribbons show almost no motion perpendicular to the PIL, which is reflected in the very slow ribbon speeds.

4.2. Correlations of the Flare-Ribbon Parameters

Figures 10 and 11 show the correlations of the characteristic flare-ribbon parameters (minimum ribbon distance, ribbon separation, and maximum ribbon-separation velocity [B_E], and E_c) as a function of the GOES class. The solid lines represent a linear fit to the individual distributions, and the corresponding correlation coefficients obtained are indicated in the left upper corner of each panel. We note that in case of a linear or log–log plot, the fit and the correlation coefficient were also calculated either in linear or log–log space. We obtained the uncertainties for the correlation coefficients using a bootstrap method. Therefore we excluded every data point once and calculated the standard deviation of all the obtained correlation coefficients. The parameters for the linear fits are listed in Table 2 of Appendix B.
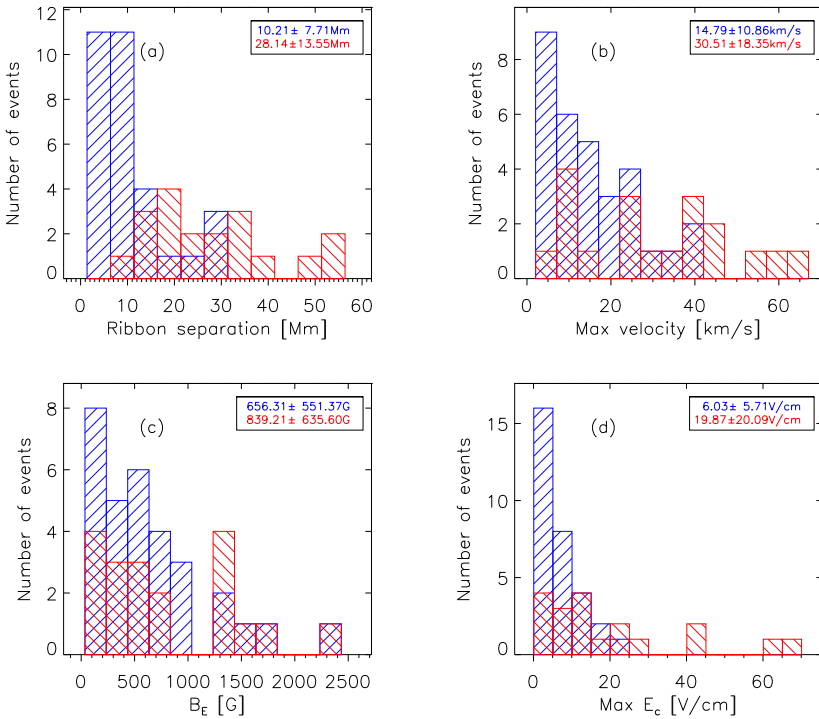
Figure 9 Distributions of the characteristic ribbon parameters of confined (*blue*; *backward diagonal hatching*) and eruptive (*red*; *forward diagonal hatching*) flares with the mean and standard deviation in the *inset*. (**a**) Ribbon separation, (**b**) maximum ribbon-separation velocity, (**c**) magnetic-field strength [B_E] at the time of the maximum electric field, and (**d**) maximum electric field.

Figure 10a shows the minimum distance as a function of the GOES flare class. Flare ribbons that do not appear *vis-à-vis* each other are represented by filled symbols. Figure 10a indicates that the initial flare-ribbon distance depends only very weakly on the GOES flux, *i.e.* the strength of the flare ($cc_{all} = 0.22 \pm 0.02$). Weak and powerful flares can have either small or large initial ribbon distances. For eruptive flares, we find a very low correlation between the initial separation and the GOES flux ($cc_{eruptive} = -0.12 \pm 0.07$), indicating that in general the former is not dependent on the latter. The correlation of the minimum distance and the GOES flux for confined flares, however, does show a trend ($cc_{confined} = 0.39 \pm 0.03$).

Figure 10b shows how the ribbon separation depends on the GOES class. Although we find a very low correlation of the ribbon separation and the flare strength for confined events ($cc_{confined} = 0.27 \pm 0.03$), the distribution is clearly separated from that of the eruptive flares. In particular, they show a lower ribbon separation for a given flare class. The ribbons of eruptive flares, on the other hand, tend to separate farther the more powerful a flare is ($cc_{eruptive} = 0.64 \pm 0.04$). Considering all flares, the same trend can be found: The ribbons of more powerful flares tend to separate farther than the ribbons of weak flares ($cc_{all} = 0.58 \pm 0.02$). However, it is important to note that this trend is mostly determined by that of the eruptive flares.

Figure 10c shows the dependence of the maximum ribbon-separation velocity on the GOES class, revealing a very weak correlation ($cc_{confined} = 0.20 \pm 0.03$, $cc_{eruptive} = 0.27 \pm 0.06$, $cc_{all} = 0.38 \pm 0.02$). The ribbon-separation velocities of both confined and eruptive
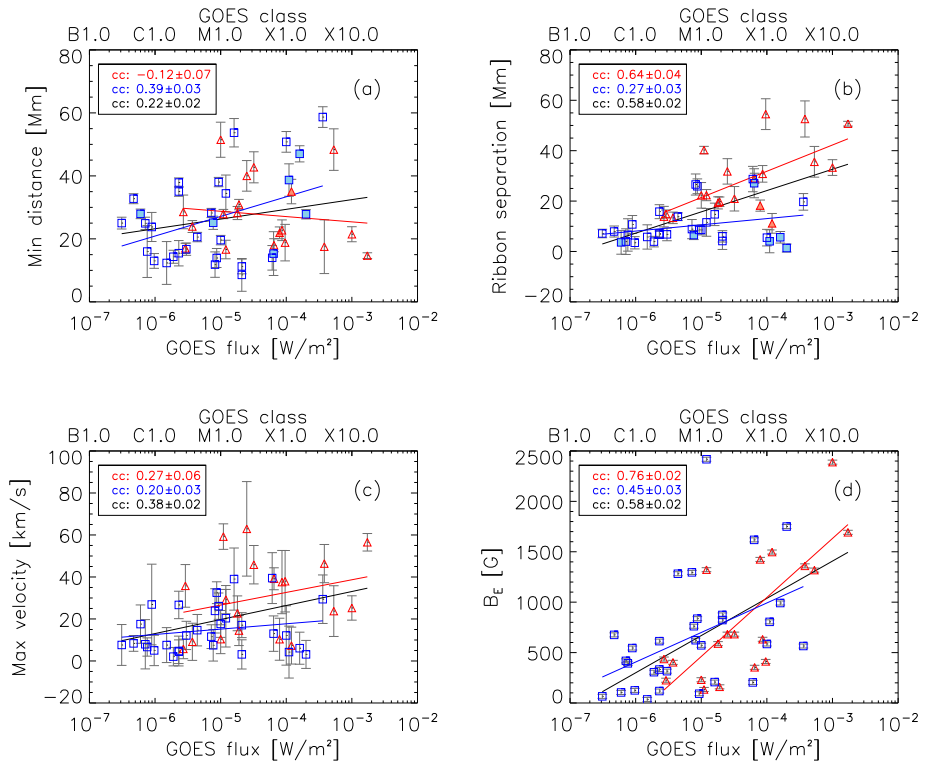
Figure 10 Dependence of the characteristic flare-ribbon parameters as a function of the GOES class. *Blue squares* correspond to confined flares and *red triangles* to eruptive flares. The *solid lines* in *red*, *blue*, and *black* represent the linear fit of eruptive, confined, and all flares (eruptive and confined), respectively. For eight flares (six confined, two eruptive), the analysis of each ribbon was done separately. These flares are represented by *filled symbols*. (**a**) Initial flare-ribbon distance, (**b**) ribbon-separation distance, (**c**) maximum ribbon-separation velocity, and (**d**) magnetic-field strength [B_E] at the time of the maximum electric field.

flares show a large dispersion. Nonetheless, a constant vertical offset of about $10 \, \mathrm{km \, s^{-1}}$ between eruptive and confined flares can be seen, indicating that the ribbons of eruptive flares tend to show higher maximum separation velocities than the ribbons of confined flares of the same class.

Figure 10d shows the magnetic field at the leading front of the flare ribbon at the time of the maximum electric field [B_E] against the GOES class. We obtain correlation coefficients of $cc_{\mathrm{confined}} = 0.45 \pm 0.03$, $cc_{\mathrm{eruptive}} = 0.76 \pm 0.02$, and $cc_{\mathrm{all}} = 0.58 \pm 0.02$, indicating that more powerful flares tend to occur in stronger magnetic fields.

Figure 11 shows the dependence of E_c on the GOES flux. It illustrates that more powerful flares reveal higher electric-field strengths, which is true for both confined and eruptive flares: $cc_{\mathrm{confined}} = 0.50 \pm 0.02$, $cc_{\mathrm{eruptive}} = 0.77 \pm 0.03$, and $cc_{\mathrm{all}} = 0.67 \pm 0.01$. The linear fits for eruptive flares are given in the form $\log(y) = 0.47 \log(x) + 3.11$, for confined flares, they are $\log(y) = 0.33 \log(x) + 2.22$, and for all flares (eruptive and confined), we find $\log(y) = 0.43 \log(x) + 2.81$.

In Figure 12 we show the correlation of E_c separately for the ribbon-separation speed and B_E, in order to evaluate which of the two quantities determine E_c more strongly. Figure 12a indicates that flares with higher maximum ribbon-separation speeds tend to have higher local

Figure 11 Dependence of the maximum electric field on the GOES class. *Blue squares* correspond to confined flares, and *red triangles* to eruptive flares. In the *bottom-right corner* we provide the equations for the linear fits.
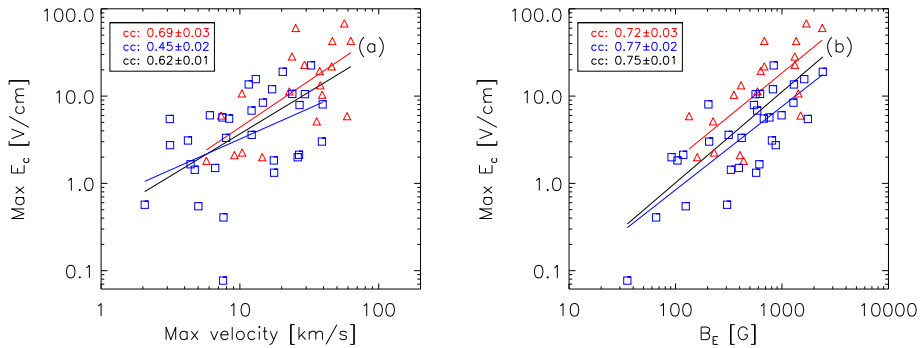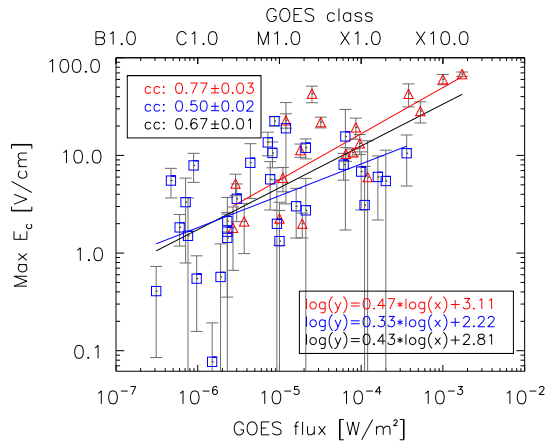
Figure 12 Dependence of the maximum electric field on the maximum ribbon-separation velocity (*left panel*) and the magnetic-field strength [B_E] at the time of the maximum electric field (*right panel*). *Blue squares* correspond to confined flares, and *red triangles* to eruptive flares.

electric-field strengths ($cc_{all} = 0.62 \pm 0.01$). This is also true when we consider confined and eruptive events separately ($cc_{confined} = 0.45 \pm 0.02$, $cc_{eruptive} = 0.69 \pm 0.03$). Considering the dependence of E_c on B_E, we find higher correlations for all of the individual samples ($cc_{confined} = 0.72 \pm 0.03$, $cc_{eruptive} = 0.77 \pm 0.02$ and $cc_{all} = 0.75 \pm 0.01$), indicating that flares occurring in regions of stronger fields tend to involve higher electric-field strengths. The constant offset in the fit curves of E_c against B_E for eruptive and confined flares can be explained by the higher ribbon-separation speeds in eruptive events.

Comparing the correlation coefficients of the reconnection electric field [E_c] as a function of maximum ribbon-separation velocity and as a function of the magnetic field swept by the ribbons, we find that the variation of the coronal electric field is more strongly affected by differences in the involved magnetic-field strength than by the ribbon-separation speed.

We also checked the flare duration for significant differences between eruptive and confined flares. Figure 13a shows the histograms of the flare duration as determined from the KSO Hα flare reports (see KSO flare start and flare end times listed in Table 1, columns 2 and 4). We find a mean flare duration of 47.2 ± 34.9 minutes for confined and 122.7 ± 77.8 minutes for eruptive flares. This finding is consistent with the results of Webb
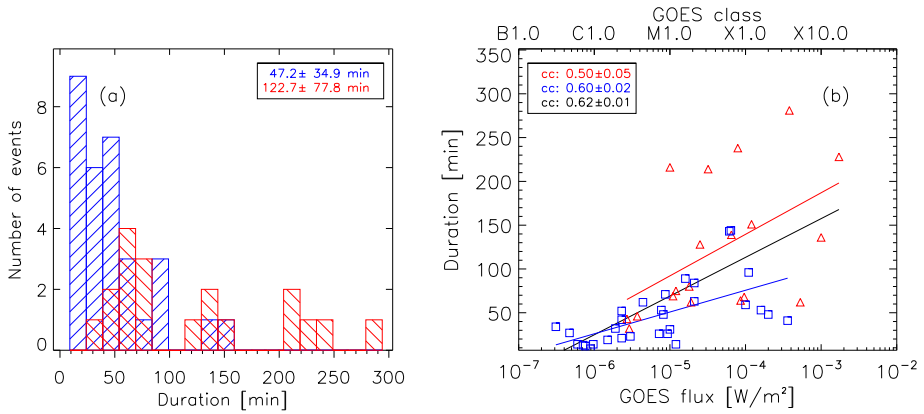
Figure 13 (**a**) Distribution of the flare duration of confined (*blue*; *backward diagonal hatching*) and eruptive (*red*, *forward diagonal hatching*) flares. The mean and standard deviation are given in the *inset*. (**b**) Dependence of flare duration on the GOES class. *Blue squares* corresponds to confined flares, and *red triangles* to eruptive flares. The *solid lines* in *red*, *blue*, and *black* represent the linear fit of eruptive, confined, and all flares (eruptive and confined), respectively.

Figure 14 Dependence of the maximum electric field on the CME velocity. In the *bottom-right corner* we provide the equation for the linear fit.
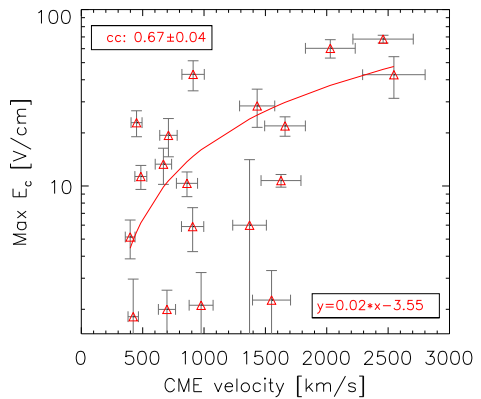
and Hundhausen (1987), who reported that flares associated with CMEs tend to be of longer duration than confined flares. In Figure 13b we plot the flare duration as a function of GOES SXR class. This plot provides further support for this finding, as the linear fits yield a vertical offset between confined and eruptive flares of about 30 minutes. However, considering the flare duration alone does not allow us to distinguish confined from eruptive flares, as the two populations of events show a significant overlap (in the range $20-100$ minutes; see Figure 13a), regardless of the flare size (compare Figure 13b).

The dependence of E_c on the speed of the associated CME is shown in Figure 14, where the uncertainty of the CME velocity is assumed to be 10%. We obtain a linear correlation coefficient of $cc = 0.67 \pm 0.04$, indicating that eruptive flares with higher electric-field strengths tend to be accompanied by faster CMEs. For the linear fit we find $E_c = -3.55 + 0.02 \, V_{CME}$.

5. Summary and Discussion

We performed a statistical study on the ribbon evolution and the coronal reconnection electric field of 50 solar flares including both confined (62%) and eruptive (38%) events, distributed over GOES classes B to > X10. We analyzed flare events that occurred from June 2000 to June 2015, homogeneously covering all Hα and GOES flare classes. Chromospheric Hα filtergrams from KSO, together with photospheric LOS magnetograms from MDI and HMI, were used to derive the flare-ribbon separation, ribbon-separation velocity, the mean magnetic-field strength, and the reconnection electric field for the individual flare events. Our main findings are summarized as follows:

- Eruptive flares reveal statistically larger ribbon separation than confined flares. Almost 70% of the confined flares but none of the eruptive flares show ribbon separation < 10 Mm. Forty percent of the eruptive flares reveal a ribbon separation > 30 Mm.
- The ribbon separation of eruptive flares correlates with the GOES flux ($cc_{\text{eruptive}} = 0.64$), indicating that more powerful eruptive flares separate farther. On the other hand, a very weak dependence of the ribbon separation on the GOES class for confined flares was found ($cc_{\text{confined}} = 0.27$).
- The maximum ribbon-separation velocity of eruptive flares shows a wide range (up to ≈ 65 km s^{-1}), whereas the majority of confined flares tends to have maximum ribbon-separation speeds < 30 km s^{-1}.
- The maximum ribbon-separation velocity of both confined and eruptive flares shows almost no correlation with the GOES class ($cc_{\text{confined}} = 0.20$, $cc_{\text{eruptive}} = 0.27$).
- The distribution of the maximum magnetic field swept by the flare ribbons for confined and eruptive flares is similar, indicating that both can appear in either weak or strong magnetic fields. B_{E} can reach values of up to almost 2500 G.
- For the most powerful eruptive flare under study, we find the highest coronal electric-field strengths [E_{c}] of up to 70 V cm^{-1}. Only one confined flare exceeds 20 V cm^{-1}, and except for four eruptive flares, E_{c} is always < 30 V cm^{-1}.
- The coronal electric field [E_{c}] shows a high correlation ($cc_{\text{confined}} = 0.50$, $cc_{\text{eruptive}} = 0.77$) with the GOES flux. Especially for confined flares, E_{c} seems to be more strongly affected by the variation in the involved magnetic field than by the ribbon-separation velocity.
- Eruptive flares tend to be of longer flare duration than confined flares (see also Webb and Hundhausen, 1987). However, there is also a pronounced overlap in the two distributions (in particular in the range $20 - 100$ minutes).
- Eruptive flares with higher E_c tend to be accompanied by faster CMEs ($cc = 0.67$)

Su, Golub, and Van Ballegooijen (2007) studied 50 confined and eruptive flares of GOES class M and X in the time range 1998 to 2005. They found that confined flares have larger initial ribbon distances and show almost no motion perpendicular to the PIL. We find that this cannot be generalized. In our extended event sample, which also includes weak confined flares, we also find small minimum distances that are comparable to the distances of eruptive flares. A clear difference might only exist for flares > M5 (see Figure 10a).

However, the ribbons of about 70% of confined flares do not separate farther than 10 Mm, which is in good agreement with the findings of Kurokawa (1989) and Su, Golub, and Van Ballegooijen (2007). A small ribbon separation in confined flares may indicate that the reconnecting current sheet cannot move upward. This does not exclude the possibility that confined events can also show a small initial ribbon distance (*cf.* Figure 10a), however, as the latter depends on the height of the reconnection region in the corona (for a recent event study see, *e.g.*, Thalmann *et al.*, 2015).

Jing *et al.* (2005) studied 13 flares (mainly M- and X-class; 11 eruptive and 2 confined) that occurred between September 2000 and March 2004 and found a linear correlation coefficient of $cc = 0.85$ for the maximum electric field and the GOES class. We obtain a similar result for the linear correlation coefficient when considering only eruptive flares ($cc_{\text{eruptive}} = 0.83 \pm 0.03$ in lin–lin space, which corresponds to $cc_{\text{eruptive}} = 0.77 \pm 0.03$ in log–lin space). Considering both confined and eruptive events, this dependence is weaker ($cc_{\text{all}} = 0.67 \pm 0.01$; see Figure 11), underlining the importance of discriminating flares in terms of their eruptivity. Jing *et al.* (2005) also related the electric field to CME velocity. Both the linear relationship between the two parameters and the correlation coefficient of the event samples match our findings well (*cf.* Figure 11 and Figure 5 of Jing *et al.*, 2005), indicating that eruptive flares with higher E_c tend to be accompanied by faster CMEs.

Toriumi *et al.* (2017) performed a statistical study of $51 \geq M5.0$ flares using AIA 1600 Å data and found a very weak correlation ($cc = 0.20$) between the GOES peak flux and the flare ribbon distance. Even though they defined the ribbon distance in a different way (geometrical centroids of the ribbons in the two polarities), the result is comparable with our study ($cc_{\text{all}} = 0.22$). However, we find that the GOES peak flux correlates better with the ribbon separation, *i.e.* how far the flare ribbons move apart from each other ($cc_{\text{all}} = 0.58$), but this trend is mostly determined by eruptive events. In an accompanying article, Tschernitz *et al.* (2017) used the same data set as in our work to study the reconnection fluxes in eruptive and confined flares. They found a similar result to that of Toriumi *et al.* (2017): confined flares of a certain GOES class have smaller ribbon areas, but larger field strengths. This is in agreement with our findings of lower ribbon-separation speeds, leading to smaller ribbon areas in confined flares.

The X3.8/3B flare on 17 January 2005 was also analyzed by Temmer *et al.* (2007). They found that the local electric-field strength is not uniform along the ribbons. They tracked the ribbons along different directions and found that the highest electric fields (up to 80 V cm^{-1}) were obtained at flare-ribbon locations where HXR footpoints are located, and the weakest electric fields (≈ 3 V cm^{-1}) were found in regions without HXR sources. For the X3.8/3B flare on 17 January 2005, we obtain ≈ 40 V cm^{-1}. Comparing the two tracking directions in Temmer *et al.* (2007) and in this study, we find that the ribbons were probably tracked along a direction that was associated with HXR footpoints.

The X10.0/2B flare on 29 October 2003 was studied by many authors (Xu *et al.*, 2004; Jing *et al.*, 2005; Krucker, Fivian, and Lin, 2005; Liu and Wang, 2009; Yang *et al.*, 2011). Table 2 in Yang *et al.* (2011) gives a summary of the reconnection electric field for this flare. The results range from 17 V cm^{-1} up to 71 V cm^{-1}, whereas the highest local electric-field strengths were obtained when tracking the location of the flare ribbons that coincide with HXR sources. Since we find $E_c = 60$ V cm^{-1} for the X10.0/2B flare on 29 October 2003, we track the Hα flare ribbons in a region of strong energy deposition.

We found a distinct correlation between the local electric field [E_c] in the reconnecting current sheet and the GOES soft X-ray flux for both confined and eruptive flares. These findings are suggestive of energetic particles that are accelerated by the electric field in the reconnecting current sheet (Litvinenko, 1996). Thus, for electrons with typical energies in the HXR range on the order of 10 to 100 keV and with the observationally determined electric fields [E_c] from 1 up to ≈ 70 keV cm^{-1} in the reconnection region, the typical length scales for the acceleration in the current sheet are 10 m to 10 km, which is consistent with the findings of Qiu *et al.* (2002). This means that a larger electric field could be responsible for higher electron acceleration in solar flares, leading to stronger emission in the X-ray regime.

Even though we find that eruptive flares reveal a statistically larger ribbon separation and higher ribbon-separation velocities, no apparent characteristic values for eruptive or confined flares are found. The reason may be that the values obtained represent local quantities, whereas the characteristics of the large-scale (global) surrounding are known to also control the eruptive behavior of flares (*e.g.* the structure and strength of the confining field; for a recent statistical study, see Baumgartner, Thalmann, and Veronig, 2017).

One may also seek to find answers on the causes and consequences during CME-associated flares, *e.g.* whether a higher E_c necessarily leads to the expulsion of a CME or whether the flare-induced formation of a CME facilitates higher E_c. Regardless of the flare type (confined or eruptive), we found that E_c is strongly correlated with the flare size (Figure 11). However, the distributions of E_c for confined and eruptive flares (Figure 9d) show a significant overlap for $E_c < 30\,\mathrm{V\,cm^{-1}}$.

If the reconnection process in confined and eruptive events were to be distinctly different, we would expect two distinctly different populations in the E_c diagrams. One may attribute the fact that we did not find such differences to the fact that we employed a local reconnection rate and that possibly existing differences might only be evident on a more global scale. However, the global peak reconnection rate determined by Tschernitz *et al.* (2017) also shows no distinction for eruptive and confined flares (see Figure 7 in Tschernitz *et al.*, 2017). This suggests that the electric field [E_c] alone is not a discriminating factor for a flare to be confined or eruptive. Based on our results, we are not able to address causes and consequences within the reconnection process in eruptive events (*i.e.* is a higher E_c a cause or a consequence of a developing CME), even more given the apparent importance of other contributing factors such as the external (confining) magnetic field surrounding the flare region, as discussed above.

Wang and Zhang (2007) studied the magnetic properties of four confined and four eruptive X-class flares in different active regions. They found that eruptive flares usually occur at the edge of an active region (AR), whereas confined flares tend to occur near the magnetic center of an AR. They also estimated for each event the magnetic flux that penetrates a vertical plane, aligned with the polarity inversion line and extending up to 1.5 solar radii (*i.e.* the horizontal flux of the confining surrounding magnetic field). Comparing the fluxes for two height regimes ($1.0-1.1\,\mathrm{R_\odot}$ and $1.1-1.5\,\mathrm{R_\odot}$), they found that the ratio of the horizontal flux in the low corona divided by that in the high corona was significantly higher for eruptive flares. The theoretical work by, *e.g.*, Török and Kliem (2005) also indicates the importance of the magnetic field surrounding the flare region in determining whether a flare is eruptive, in particular the decay index [n] of the magnetic field, which is defined as the logarithmic decay of the horizontal component of the confining magnetic field above the axis of a possibly unstable flux rope. The flux system will erupt if n exceeds a critical value (*e.g.* Kliem and Török, 2006; Zuccarello, Aulanier, and Gilchrist, 2015), implying that an overlying field that decays in strength more slowly with height may result in a flare without an associated CME. This is in agreement with Sun *et al.* (2015), who analyzed three active regions and found that for the flare-rich but CME-poor AR 12192, the critical value of the decay index is reached much higher in the corona than for the CME-producing active regions.

In order to shed more light on the reconnection process of solar flares, combined measurements from spacecraft at different positions in the heliosphere would be helpful. Recently, case studies using the *Atmospheric Imaging Assembly* (AIA) and the *Ramaty High Energy Solar Spectroscopic Imager* (RHESSI) have been performed where magnetic reconnection could directly be observed (*e.g.* Su *et al.*, 2013; Gou *et al.*, 2017). The signatures of

magnetic reconnection, such as plasma inflow to the current sheet, reconnection outflows, associated energy release in form of plasma heating, and particle acceleration, are best observed on the solar limb. However, in these cases we cannot measure the magnetic field, which is the crucial parameter in the physics of the events. Thus spacecraft positioned at L_5 or L_4 in addition to spacecraft at L_1 (and ground-based observations) including magnetographs at all spacecraft may provide a great step forward in better determining the governing physical processes from the observations.

Disclosure of Potential Conflicts of Interest The authors declare that they have no conflicts of interest.

Appendix A: Fitting a Gaussian Function to the Intensity Profiles

In order to determine the leading front of the flare ribbons, we fitted a Gaussian function to the Hα flare ribbon intensity profiles (*cf.* Figure 3). The Gaussian function is defined as

$$y(x) = A_0 \exp\left[-0.5\left(\frac{x - A_1}{A_2}\right)^2\right], \tag{4}$$

where A_0 is the peak value of the fit function, A_1 is the centroid, and A_2 is the standard deviation of the Gaussian function. The peak position $[x_\mathrm{p}]$ and the leading front position $[x_\mathrm{l}]$ are defined to be functions of the parameters of the Gaussian fit:

$$x_\mathrm{p} = A_1, \tag{5}$$

$$x_\mathrm{l} = A_1 + 2A_2. \tag{6}$$

The uncertainty of the peak position is defined as

$$\Delta x_\mathrm{p} = \pm\mathrm{Max}(1\mathrm{pix}, \Delta p_1), \tag{7}$$

where Δp_1 is the uncertainty on the parameter A_1, *i.e.* the centroid position of the peak. Therefore, it is at least one pixel, assumed as the minimum error due to atmospheric and seeing conditions, but it may also be larger depending on Δp_1. The uncertainty of the leading front position is defined as

$$\Delta x_\mathrm{f} = \pm(\Delta x_\mathrm{p} + 2\Delta p_2), \tag{8}$$

where Δp_2 is the uncertainty of the parameter A_2, *i.e.* the standard deviation of the Gaussian function.

Table 2 Correlation coefficients and parameters of the linear fits for confined, eruptive, and all (confined and eruptive) flares for the particular scatter plots shown in Figure 10 – 14. Note that some fits are applied in lin–log space and some in log–log space.

Figure	Confined	Eruptive	All
Figure 10a	$cc = 0.39 \pm 0.03$	$cc = -0.12 \pm 0.07$	$cc = 0.22 \pm 0.02$
	$y = 6.23 \log(x) + 58.29$	$y = -1.68 \log(x) + 20.38$	$y = 3.08 \log(x) + 41.70$
Figure 10b	$cc = 0.27 \pm 0.03$	$cc = 0.64 \pm 0.04$	$cc = 0.58 \pm 0.02$
	$y = 2.48 \log(x) + 22.96$	$y = 10.42 \log(x) + 73.52$	$y = 8.45 \log(x) + 57.99$
Figure 10c	$cc = 0.20 \pm 0.03$	$cc = 0.27 \pm 0.06$	$cc = 0.38 \pm 0.02$
	$y = 2.54 \log(x) + 27.88$	$y = 6.03 \log(x) + 56.75$	$y = 6.68 \log(x) + 53.11$
Figure 10d	$cc = 0.45 \pm 0.03$	$cc = 0.762 \pm 0.02$	$cc = 0.58 \pm 0.02$
	$y = 292.86 \log(x) + 2163.52$	$y = 585.30 \log(x) + 3387.87$	$y = 369.29 \log(x) + 2515.24$
Figure 11	$cc = 0.50 \pm 0.02$	$cc = 0.77 \pm 0.03$	$cc = 0.67 \pm 0.01$
	$\log(y) = 0.33 \log(x) + 2.22$	$\log(y) = 0.47 \log(x) + 3.11$	$\log(y) = 0.43 \log(x) + 2.81$
Figure 12a	$cc = 0.45 \pm 0.02$	$cc = 0.69 \pm 0.03$	$cc = 0.62 \pm 0.01$
	$\log(y) = 0.71 \log(x) - 0.20$	$\log(y) = 1.07 \log(x) - 0.43$	$\log(y) = 0.96 \log(x) - 0.4$
Figure 12b	$cc = 0.77 \pm 0.02$	$cc = 0.72 \pm 0.03$	$cc = 0.75 \pm 0.01$
	$\log(y) = 0.96 \log(x) - 1.98$	$\log(y) = 1.00 \log(x) - 1.73$	$\log(y) = 1.04 \log(x) - 2.08$
Figure 13b	$cc = 0.60 \pm 0.02$	$cc = 0.50 \pm 0.05$	$cc = 0.62 \pm 0.01$
	$y = 24.9 \log(x) + 175.1$	$y = 47.4 \log(x) + 329.3$	$y = 44.2 \log(x) + 290.1$
Figure 14	–	$cc = 0.70 \pm 0.04$	–
	–	$y = 0.02\,x - 6.62$	–

Appendix B: Parameters of the Linear Fits

Table 2 contains the parameters of the linear fits for all correlation plots.

References

Asai, A., Yokoyama, T., Shimojo, M., Masuda, S., Kurokawa, H., Shibata, K.: 2004, Flare ribbon expansion and energy release rate. *Astrophys. J.* **611**, 557. DOI. ADS.

Aschwanden, M.J.: 2005, *Physics of the Solar Corona. an Introduction with Problems and Solutions*, 2nd edn. Springer, Berlin. ADS.

Aulanier, G., Janvier, M., Schmieder, B.: 2012, The standard flare model in three dimensions. I. Strong-to-weak shear transition in post-flare loops. *Astron. Astrophys.* **543**, A110. DOI. ADS.

Baumgartner, C., Thalmann, J.K., Veronig, A.M.: 2017, On the factors determining the eruptive character of solar flares. arXiv. ADS.

Carmichael, H.: 1964, A process for flares. In: Hess, W.N. (ed.) *The Physics of Solar Flares* **SP-50**, NASA, Washington, 451. ADS.

Emslie, A.G.: 2003, The determination of the total injected power in solar flare electrons. *Astrophys. J. Lett.* **595**, L119. DOI. ADS.

Fletcher, L., Dennis, B.R., Hudson, H.S., Krucker, S., Phillips, K., Veronig, A., Battaglia, M., Bone, L., Caspi, A., Chen, Q., Gallagher, P., Grigis, P.T., Ji, H., Liu, W., Milligan, R.O., Temmer, M.: 2011, An observational overview of solar flares. *Space Sci. Rev.* **159**, 19. DOI. ADS.

Forbes, T.G., Lin, J.: 2000, What can we learn about reconnection from coronal mass ejections? *J. Atmos. Solar-Terr. Phys.* **62**, 1499. DOI. ADS.

Forbes, T.G., Priest, E.R.: 1984, Reconnection in solar flares. In: Butler, D.M., Papadopoulos, K.N. (eds.) *Solar Terrestrial Physics: Present and Future*, **RP-1120**, NASA, Washington, 1.

Gou, T., Veronig, A.M., Dickson, E.C., Hernandez-Perez, A., Liu, R.: 2017, Direct observation of two-step magnetic reconnection in a solar flare. *Astrophys. J. Lett.* **845**, L1. DOI. ADS.

Hirayama, T.: 1974, Theoretical model of flares and prominences. I: evaporating flare model. *Solar Phys.* **34**, 323. DOI. ADS.

Janvier, M., Aulanier, G., Bommier, V., Schmieder, B., Démoulin, P., Pariat, E.: 2014, Electric currents in flare ribbons: observations and three-dimensional standard model. *Astrophys. J.* **788**, 60. DOI. ADS.

Jing, J., Qiu, J., Lin, J., Qu, M., Xu, Y., Wang, H.: 2005, Magnetic reconnection rate and flux-rope acceleration of two-ribbon flares. *Astrophys. J.* **620**, 1085. DOI. ADS.

Kliem, B., Török, T.: 2006, Torus instability. *Phys. Rev. Lett.* **96**(25), 255002. DOI. ADS.

Kopp, R.A., Pneuman, G.W.: 1976, Magnetic reconnection in the corona and the loop prominence phenomenon. *Solar Phys.* **50**, 85. DOI. ADS.

Krucker, S., Fivian, M.D., Lin, R.P.: 2005, Hard X-ray footpoint motions in solar flares: comparing magnetic reconnection models with observations. *Adv. Space Res.* **35**, 1707. DOI. ADS.

Kurokawa, H.: 1989, High-resolution observations of H-alpha flare regions. *Space Sci. Rev.* **51**, 49. DOI. ADS.

Litvinenko, Y.E.: 1996, Particle acceleration in reconnecting current sheets with a nonzero magnetic field. *Astrophys. J.* **462**, 997. DOI. ADS.

Litvinenko, Y.E., Somov, B.V.: 1995, Relativistic acceleration of protons in reconnecting current sheets of solar flares. *Solar Phys.* **158**, 317. DOI. ADS.

Liu, C., Wang, H.: 2009, Reconnection electric field and hardness of X-ray emission of solar flares. *Astrophys. J. Lett.* **696**, L27. DOI. ADS.

Martens, P.C.H., Young, A.: 1990, Neutral beams in two-ribbon flares and in the geomagnetic tail. *Astrophys. J. Suppl.* **73**, 333. DOI. ADS.

Miklenic, C.H., Veronig, A.M., Vršnak, B., Hanslmeier, A.: 2007, Reconnection and energy release rates in a two-ribbon flare. *Astron. Astrophys.* **461**, 697. DOI. ADS.

Neidig, D., Wiborg, P., Confer, M., Haas, B., Dunn, R., Balasubramaniam, K.S., Gullixson, C., Craig, D., Kaufman, M., Hull, W., McGraw, R., Henry, T., Rentschler, R., Keller, C., Jones, H., Coulter, R., Gregory, S., Schimming, R., Smaga, B.: 1998, The USAF Improved Solar Observing Optical Network (ISOON) and its impact on solar synoptic data bases. In: Balasubramaniam, K.S., Harvey, J., Rabin, D. (eds.) *Synoptic Solar Physics*, **CP-140**, Astron. Soc. Pacific, San Francisco, 519. ADS.

Neupert, W.M.: 1968, Comparison of solar X-ray line emission with microwave emission during flares. *Astrophys. J. Lett.* **153**, L59. DOI. ADS.

Poletto, G., Kopp, R.A.: 1986, Macroscopic electric fields during two-ribbon flares. In: Neidig, D.F. (ed.) *The Lower Atmosphere of Solar Flares; Proc. Solar Maximum Mission Symp.*, NSO, Sunspot, 453. ADS.

Pötzi, W., Veronig, A.M., Riegler, G., Amerstorfer, U., Pock, T., Temmer, M., Polanec, W., Baumgartner, D.J.: 2015, Real-time flare detection in ground-based Hα imaging at Kanzelhöhe Observatory. *Solar Phys.* **290**, 951. DOI. ADS.

Qiu, J., Lee, J., Gary, D.E., Wang, H.: 2002, Motion of flare footpoint emission and inferred electric field in reconnecting current sheets. *Astrophys. J.* **565**, 1335. DOI. ADS.

Scherrer, P.H., Bogart, R.S., Bush, R.I., Hoeksema, J.T., Kosovichev, A.G., Schou, J., Rosenberg, W., Springer, L., Tarbell, T.D., Title, A., Wolfson, C.J., Zayer, I., MDI Engineering Team: 1995, The solar oscillations investigation – Michelson Doppler imager. *Solar Phys.* **162**, 129. DOI. ADS.

Schou, J., Scherrer, P.H., Bush, R.I., Wachter, R., Couvidat, S., Rabello-Soares, M.C., Bogart, R.S., Hoeksema, J.T., Liu, Y., Duvall, T.L., Akin, D.J., Allard, B.A., Miles, J.W., Rairden, R., Shine, R.A., Tarbell, T.D., Title, A.M., Wolfson, C.J., Elmore, D., Norton, A.A., Tomczyk, S.: 2012, Design and ground calibration of the Helioseismic and Magnetic Imager (HMI) instrument on the Solar Dynamics Observatory (SDO). *Solar Phys.* **275**, 229. DOI. ADS.

Sturrock, P.A.: 1966, Model of the high-energy phase of solar flares. *Nature* **211**, 695. DOI. ADS.

Su, Y., Golub, L., Van Ballegooijen, A.A.: 2007, A statistical study of shear motion of the footpoints in two-ribbon flares. *Astrophys. J.* **655**, 606. DOI. ADS.

Su, Y., Veronig, A.M., Holman, G.D., Dennis, B.R., Wang, T., Temmer, M., Gan, W.: 2013, Imaging coronal magnetic-field reconnection in a solar flare. *Nat. Phys.* **9**, 489. DOI. ADS.

Sun, X., Bobra, M.G., Hoeksema, J.T., Liu, Y., Li, Y., Shen, C., Couvidat, S., Norton, A.A., Fisher, G.H.: 2015, Why is the great solar active region 12192 flare-rich but CME-poor? *Astrophys. J. Lett.* **804**, L28. DOI. ADS.

Švestka, Z.: 1986, On the varieties of solar flares. In: Neidig, D.F. (ed.) *The Lower Atmosphere of Solar Flares; Proceedings of the Solar Maximum Mission Symp.* NSO, Sunspot, 332. ADS.

Temmer, M., Veronig, A.M., Vršnak, B., Miklenic, C.: 2007, Energy release rates along Hα flare ribbons and the location of hard X-ray sources. *Astrophys. J.* **654**, 665. DOI. ADS.

Temmer, M., Thalmann, J.K., Dissauer, K., Veronig, A.M., Tschernitz, J., Hinterreiter, J., Rodriguez, L.: 2017, On flare-CME characteristics from Sun to Earth combining remote-sensing image data with in situ measurements supported by modeling. *Solar Phys.* **292**, 93. DOI. ADS.

Thalmann, J.K., Su, Y., Temmer, M., Veronig, A.M.: 2015, The confined X-class flares of solar active region 2192. *Astrophys. J. Lett.* **801**, L23. DOI. ADS.

Toriumi, S., Schrijver, C.J., Harra, L.K., Hudson, H., Nagashima, K.: 2017, Magnetic properties of solar active regions that govern large solar flares and eruptions. *Astrophys. J.* **834**, 56. DOI. ADS.

Török, T., Kliem, B.: 2005, Confined and ejective eruptions of kink-unstable flux ropes. *Astrophys. J. Lett.* **630**, L97. DOI. ADS.

Tschernitz, J., Veronig, A.M., Thalmann, J.K., Hinterreiter, J., Pötzi, W.: 2017, Reconnection fluxes in eruptive and confined flares and implications for superflares on the Sun. arXiv. ADS.

Veronig, A.M., Polanec, W.: 2015, Magnetic reconnection rates and energy release in a confined X-class flare. *Solar Phys.* **290**, 2923. DOI. ADS.

Veronig, A.M., Brown, J.C., Dennis, B.R., Schwartz, R.A., Sui, L., Tolbert, A.K.: 2005, Physics of the Neupert effect: estimates of the effects of source energy, mass transport, and geometry using RHESSI and GOES data. *Astrophys. J.* **621**, 482. DOI. ADS.

Vršnak, B.: 1990, Eruptive instability of cylindrical prominences. *Solar Phys.* **129**, 295. DOI. ADS.

Wang, Y., Zhang, J.: 2007, A comparative study between eruptive X-class flares associated with coronal mass ejections and confined X-class flares. *Astrophys. J.* **665**, 1428. DOI. ADS.

Webb, D.F., Hundhausen, A.J.: 1987, Activity associated with the solar origin of coronal mass ejections. *Solar Phys.* **108**, 383. DOI. ADS.

Xu, Y., Cao, W., Liu, C., Yang, G., Qiu, J., Jing, J., Denker, C., Wang, H.: 2004, Near-infrared observations at 1.56 microns of the 2003 October 29 X10 white-light flare. *Astrophys. J. Lett.* **607**, L131. DOI. ADS.

Yang, Y.-H., Cheng, C.Z., Krucker, S., Hsieh, M.-S.: 2011, Estimation of the reconnection electric field in the 2003 October 29 X10 flare. *Astrophys. J.* **732**, 15. DOI. ADS.

Yashiro, S., Akiyama, S., Gopalswamy, N., Howard, R.A.: 2006, Different power-law indices in the frequency distributions of flares with and without coronal mass ejections. *Astrophys. J. Lett.* **650**, L143. DOI. ADS.

Zuccarello, F.P., Aulanier, G., Gilchrist, S.A.: 2015, Critical decay index at the onset of solar eruptions. *Astrophys. J.* **814**, 126. DOI. ADS.